European Journal of Organic Chemistry

EurJOC
European Journal of Organic Chemistry

Chemistry Europe
European Chemical Societies Publishing

RESEARCH ARTICLE

Sterically Crowded Hexaterpyridyl–BODIPY: A Multiresponsive Far-Red Emissive AIE-Active Probe for Zn(II) Recognition and Biological Applications

Kanhu Charan Behera[1,2] | Suprava Das[3]

[1]Department of Chemistry and Center for Emerging Materials and Advanced Devices, National Taiwan University, Taipei, Taiwan | [2]CSIR-Institute of Minerals and Material Technology (CSIR-IMMT), Bhubaneswar, India | [3]Department of Chemical and Materials Engineering, Chang Gung University, Taoyuan, Taiwan

Correspondence: Kanhu Charan Behera (kanhu.chem@gmail.com)

Received: 16 April 2026 | **Revised:** 5 June 2026 | **Accepted:** 12 June 2026

Keywords: BODIPY | BODIPY–terpyridyl conjugates | multiresponsive | sterically crowded | terpyridyl

ABSTRACT

Sterically crowded aggregation-induced emission (AIE)-active fluorophores provide a powerful approach to constructing multifunctional platforms for sensing and bioimaging. Herein, we describe the rational design and synthesis of a highly crowded hexaterpyridyl-functionalized BODIPY, obtained through hexabromination of the BODIPY core followed by Suzuki–Miyaura coupling with terpyridyl boronic acid derivatives. Spectroscopic characterization confirms the structure, while the installation of six terpyridine units at the α/β positions generates substantial steric crowding, leading to pronounced AIE behavior, far-red emission, cooperative metal-ion coordination, and efficient cellular imaging. Systematic aggregation studies in THF/water mixtures reveal significant fluorescence enhancement correlated with the formation of well-defined spherical nanoaggregates, as confirmed by TEM and SEM analyses. The hexaterpyridyl–BODIPY further exhibits selective Zn(II) recognition with distinct fluorescence responses. Comparative studies with α,α- and β,β-diterpyridyl analogs emphasize the critical role of multiligand steric crowding in tuning aggregation, photophysical properties, and biological performance. Notably, the hexaterpyridyl derivative shows efficient cellular uptake, bright intracellular fluorescence, excellent biocompatibility in normal and cancer cell lines, and enhanced phototoxicity compared to its counterparts. DFT calculations elucidate the structure–property relationships, establishing a versatile molecular design strategy that integrates AIE, metal-ion sensing, and bioimaging within a single BODIPY scaffold.

1 | Introduction

The rational design of multifunctional fluorescent platforms that integrate metal-ion recognition, stimulus responsiveness, and bioimaging capability remains a central goal in contemporary supramolecular and materials chemistry [1–5]. Among the wide variety of organic fluorophores, boron-dipyrromethene (BODIPY) dyes represent one of the most versatile classes owing to their sharp absorption bands, high fluorescence quantum yields, tunable spectral profiles, and excellent photostability. As a result, BODIPY derivatives have found widespread applications as biomolecular labels, chromogenic probes, cation sensors, drug delivery agents, fluorescent switches, photosensitizers for solar cells, and bioimaging agents [6–10]. However, conventional BODIPY systems frequently suffer from aggregation-caused quenching (ACQ) in the solid or aggregated state, significantly limiting their performance in complex biological and aqueous environments. Substitution around the BODIPY core provides a powerful strategy for modulating electronic, photophysical, and electrochemical properties. Nevertheless, functionalization at all six pyrrolic carbon positions remains synthetically challenging, and only a limited number of reports [11–14] describe sterically crowded hexaaryl-substituted BODIPYs (Scheme 1), with both symmetrical and asymmetrical substitution patterns being rare

Dedicated to Professor Mangalampalli Ravikanth on his 60th birthday.

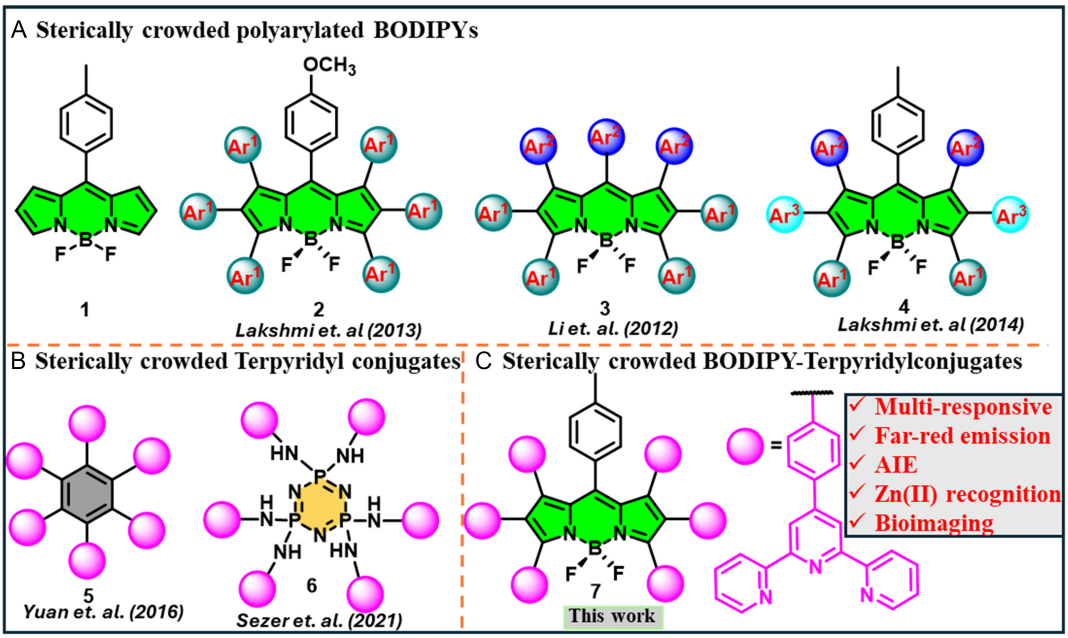

SCHEME 1 | Structure of BODIPY along with sterically crowded polyarylated BODIPYs (A) and sterically crowded terpyridyl conjugates (B) reported in literature, along with BODIPY conjugate (C) (this work).

despite their potential to induce structural distortion and improve emission properties.

Aggregation-induced emission (AIE) has emerged as an effective approach to overcome ACQ, enabling luminogens that are weakly emissive in solution but highly fluorescent upon aggregation [15, 16]. Introducing steric congestion and conformational restriction into fluorophore frameworks suppresses nonradiative decay pathways by restricting intramolecular motion (RIM), thereby promoting enhanced emission in the aggregated state [17, 18]. Sterically crowded architectures also generate dynamic molecular environments that respond to external stimuli such as metal ions, solvent polarity, and mechanical stress. These characteristics have stimulated extensive research into functional AIE-active materials for sensing, bioimaging, and optoelectronic applications [15–18].

Terpyridine is a privileged ligand in coordination chemistry owing to its predictable coordination geometry, rich redox behavior, and modular functionalization; thus, it has been widely employed in molecular sensors, supramolecular gels, metallosupramolecular assemblies, and stimuli-responsive materials [19–24]. Zn(II) is a biologically essential yet spectroscopically silent metal ion that plays crucial roles in enzymatic catalysis, gene regulation, and neuronal signaling. Consequently, the development of efficient fluorescent probes for Zn(II) detection remains of significant interest in both chemical analysis and biological imaging. Terpyridine ligands offer an attractive platform for functionalizing luminescent scaffolds. Their rigid π-conjugated backbone, substantial steric bulk, and multiple coordination sites not only disrupt detrimental intermolecular packing but also facilitate supramolecular assembly toward aggregation-induced emission [25–28]. Terpyridine efficiently recognizes Zn(II) through its tridentate nitrogen-donor framework, which prevents fluorescence quenching, often resulting in enhanced emission via intramolecular charge transfer (ICT) or restricted molecular motion. Despite the extensive use of multiterpyridine ligands in hexa-terpyridyl multiruthenium complexes [29] and metallo-supramolecular polymers [30], their systematic integration into BODIPY frameworks remains largely unexplored. Unlike simple phenyl, pyridyl, or alkyl substituents, which provide limited steric hindrance, terpyridyl groups introduce substantial steric crowding together with metal-binding functionality. Such structural features were therefore envisioned as a dual-purpose strategy to suppress ACQ and promote AIE behavior.

Integrating multiple terpyridine units onto a compact BODIPY core presents both opportunities and challenges. Nevertheless, highly congested multi-terpyridyl–BODIPY systems are rare, particularly those exhibiting AIE and metal-ion-responsive fluorescence. Herein, we report the design and synthesis of a sterically crowded hexaterpyridyl–BODIPY architecture **7** (Scheme 1) that functions as a multiresponsive fluorescent platform. The presence of six terpyridine units around the BODIPY core induces pronounced steric hindrance, leading to AIE behavior. Furthermore, the cooperative coordination of terpyridine sites enables selective and sensitive recognition of Zn(II), accompanied by distinct optical responses. Again, the hexaterpyridyl–BODIPY **7** demonstrates excellent performance in cellular bioimaging, with enhanced phototoxic effects attributed to increased photodynamic therapy (PDT)-mediated cellular damage. Overall, this work establishes a new design paradigm for sterically congested, multiligand fluorophores that synergistically combine AIE activity, metal-ion sensing, and bioimaging functionality, offering new opportunities for advanced applications in supramolecular chemistry, optoelectronics, and biomedical diagnostics.

2 | Results and Discussion

As illustrated in Scheme 2, the synthesis of the hexaterpyridyl-coupled BODIPY derivative **7** was initiated from the parent

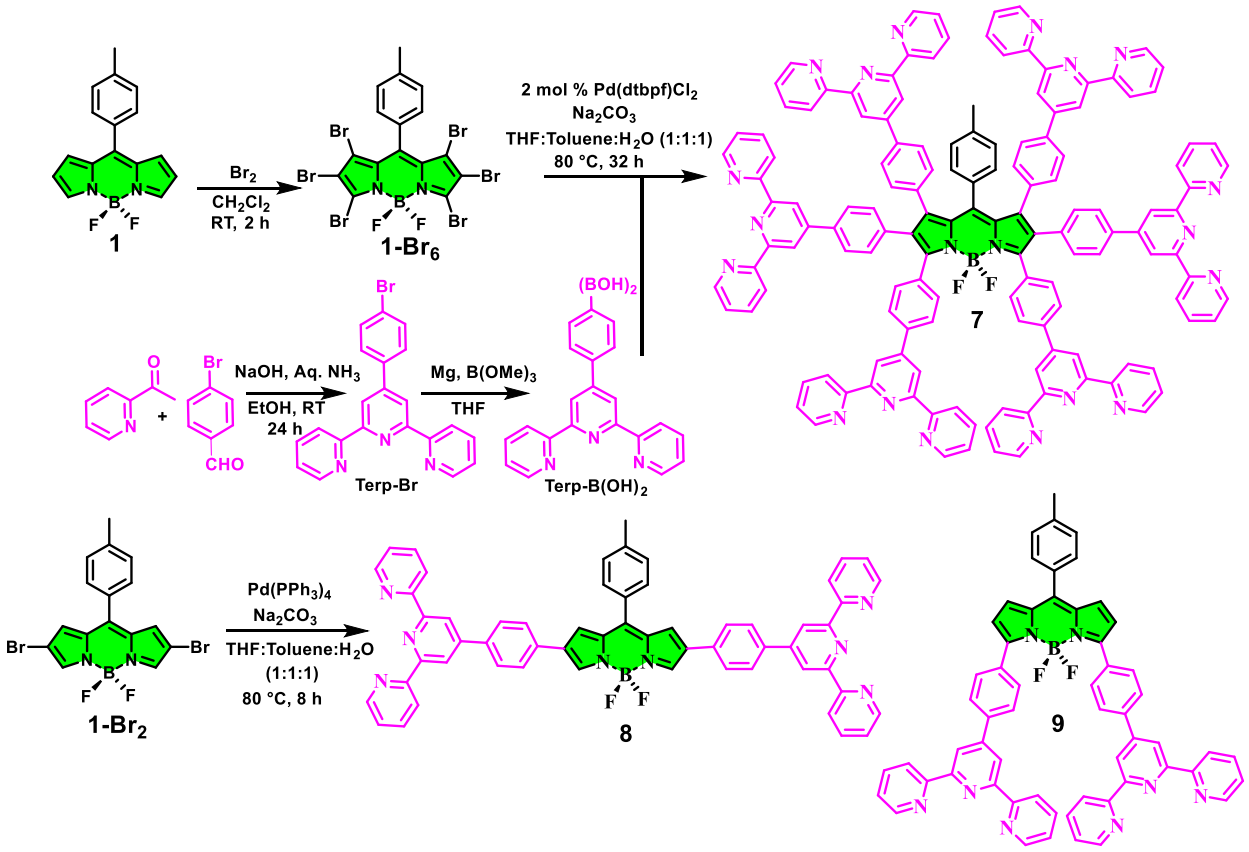

SCHEME 2 | Synthesis of covalently linked hexa-terpyridyl–BODIPY **7** and α,α-di(terpyridyl)–BODIPY **8** and β,β-di(terpyridyl)–BODIPY **9**.

BODIPY core, which underwent hexabromination to afford the corresponding hexabrominated BODIPY intermediate. Subsequent Suzuki–Miyaura coupling of this intermediate with *Terp*-$B(OH)_2$ in the presence of a catalytic amount of [*Bis*(*di-tert-butylphosphino*)*ferrocene*]*palladium*(*II*) *dichloride* [31] and Na_2CO_3 in *toluene:THF:*H_2O (*1:1:1*) mixture furnished the hexa-terpyridyl–BODIPY **7** as a green solid in 25% yield. The structure of compound **7** was unambiguously confirmed by high-resolution mass spectrometry and NMR spectroscopy (Figures S1–S5). For comparison, two regioselective control analogs α,α-di(terpyridyl)–BODIPY **8** and β,β-di(terpyridyl)–BODIPY **9** were synthesized starting from the corresponding α,α-dibromo–BODIPY and β,β-dibromo–BODIPY precursors. These intermediates were subjected to a $Pd(PPh_3)_4$-catalyzed Suzuki coupling with terpyridyl boronic acid in the presence of Na_2CO_3, affording compounds **8** and **9** in 40% and 34% yields, respectively, both of which were fully characterized (Figures S6–S11).

The absorption and fluorescence spectra of compounds **7**–**9** were recorded in CH_2Cl_2 solution (Figure 1a,b). For reference, the parent BODIPY chromophore exhibited a strong absorption maximum at 499 nm (with a shoulder at 480 nm) and an emission band centered at 515 nm. In contrast, compound **7** displayed a pronounced bathochromic shift with an absorption maximum at 650 nm (Figure 1a), indicative of extensive π-conjugation throughout the six terpyridyl framework, allowing for extensive overlap of π orbitals between the BODIPY chromophore and peripheral terpyridine ligands. Compounds **8** and **9** exhibited intense absorption bands at 600 nm and 577 nm, respectively, which can similarly be attributed to extended electronic delocalization through α,α-diterpyridyl–BODIPY and β,β-diterpyridyl–BODIPY. All terpyridyl–BODIPY conjugates **7**–**9** were emissive in the visible–near-infrared region. Compound **7** emitted strongly at 670 nm with a quantum yield of 0.23, whereas **8** and **9** showed emission maxima at 630 nm and 613 nm, respectively (Figure 1b), with fluorescence quantum yields (Φ_F) of 0.45 and 0.63. The pronounced far-red emission of **7** arises from extensive π-conjugation and ICT between the electron-rich BODIPY core and electron-deficient terpyridyl substituents.

To understand the aggregation properties of **7**, the fluorescence intensity was measured in a THF/water mixture by varying the fraction of water in THF (Figure 1c). For instance, **7** showed a maximum emission band at 670 nm with red emission and a quantum yield of 0.23. Subsequently, upon increasing the water fraction, it was noticed that with increasing water fraction from 0% to 70%, the fluorescence spectra became broader, showing an emission peak at 670 nm without any significant shift in wavelength, and the F.I. was about 2.5-fold higher than I_0. Further increasing the water fraction up to 90%, the emission peak exhibited a 10 nm blue shift with an enhancement in the emission band with a quantum yield of 0.49. However, when the water content was raised to $f_w = 95\%$, the fluorescence intensity decreased, which can be ascribed to excessive aggregation and partial exciton annihilation [32–34]. In comparison, the diterpyridyl BODIPY derivatives **8** and **9** exhibited markedly different photophysical behavior under identical conditions. Increasing the water fraction in THF solutions of di-terpyridyl BODIPY derivatives **8** and **9** (Figure S12) produced only negligible changes in both emission wavelength and fluorescence intensity, indicating the absence of significant

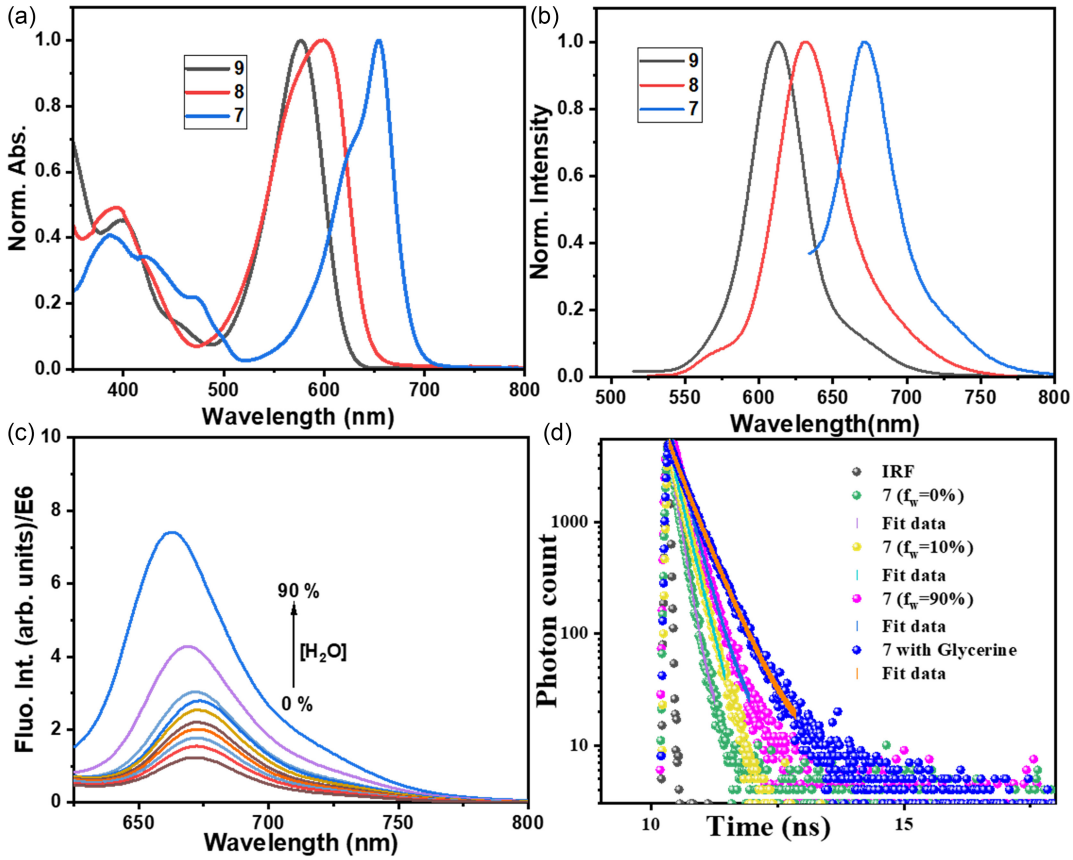

FIGURE 1 | Comparison of (a) absorption spectra and (b) emission spectra of compounds **7–9**, and (c) fluorescence spectrum of **7** in THF with different variation of H_2O (d) fluorescence decay profile of **7** in THF with different variation of H_2O and glycerin (concentrations used: [**7–9**] = 10 μM [for absorption] and 1 μM [for emission]).

AIE behavior as compared to **7**. This contrasting response can be attributed to their lower molecular rigidity, greater conformational flexibility, and reduced steric hindrance compared to the hexasubstituted analog. The less congested structures in **8** and **9** facilitate stronger intermolecular π–π interactions in the aggregated state, leading to weakly emissive aggregates rather than enhanced fluorescence. These observations underscore the critical influence of peripheral substitution and conformational restriction in modulating the aggregation-dependent emissive properties of BODIPY-based systems.

Fluorescence lifetime measurements provided deeper insight into the emission process. The singlet-state lifetime of **7** (Figure 1d) in pure THF ($f_w = 0\%$) exhibited a mono-exponential decay with a lifetime of 1.14 ns. Upon increasing the water fraction, the lifetime gradually increased to 1.24 ns at $f_w = 10\%$, and further to 1.33 ns in the aggregated state ($f_w = 90\%$). Upon aggregation, the intramolecular rotation of the six bulky terpyridyl groups is restricted, which suppresses nonradiative decay pathways. This also creates strong steric congestion and conformational locking, resulting in a longer fluorescence lifetime and enhanced emission. To further corroborate the RIM mechanism, fluorescence lifetime measurements were performed in a highly viscous glycerol medium, where a pronounced increase in lifetime was observed (1.51 ns) compared to both the solution and aggregated states. These results collectively confirm that compound **7** exhibits efficient AIE characteristics with strong red emission, highlighting its potential as a promising material for bioimaging applications. In addition, as a supplementary control study, the temperature-dependent emission behavior of compounds **7–9** under AIE conditions was investigated. Notably, compound **7** exhibited a significantly greater temperature sensitivity than compounds **8** and **9**, with its emission intensity decreasing markedly upon increasing temperature. This observation suggests that the emissive aggregated state of compound **7** is more strongly governed by restricted intramolecular motions and intermolecular interactions arising from its densely packed hexaterpyridyl framework. In contrast, the corresponding changes in compounds **8** and **9** were considerably less pronounced.

To understand the nature of aggregation in **7**, the morphology of the aggregates was obtained from SEM analysis of aggregated samples deposited on carbon tape after drying. As shown in Figure 2a,b, compound **7** exhibits a well-defined spherical morphology in its aggregated form at 0% water fraction (Figure 2a). Upon increasing the water content to 90%, the spherical morphology is retained; however, the particle size decreases due to rapid aggregate formation under high water content (Figure 2b). Further insight was obtained from TEM analysis of aggregates formed at a concentration of 100 μM in 10% THF/90% H_2O, prepared by drop-casting the solution onto carbon-coated copper grids (Figure 2c,d). Due to the presence of six terpyridyl substituents around the BODIPY core, intermolecular interactions of **7** were so strong and allowed the formation of structurally well-defined spherical aggregates in **7**. The compound **7** self-assembled into regular nanospheres at 0% of water (Figure 2c). However,

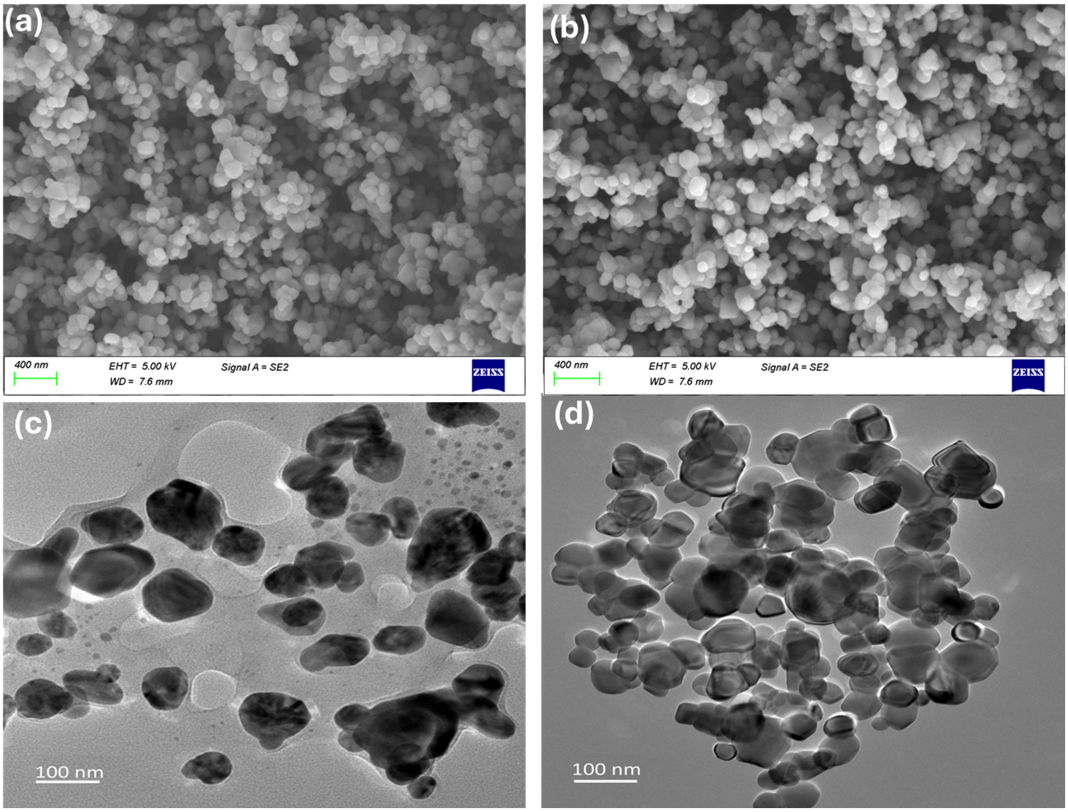

FIGURE 2 | SEM images of aggregates of compound **7** formed in THF/H_2O mixtures at different water fractions: (a) 0% H_2O and (b) 90% H_2O. TEM images of the corresponding aggregates: (c) 0% H_2O and (d) 90% H_2O in THF (10^{-4} M concentration).

when the water fraction was increased substantially (90%), the rapid formation of the aggregates led to the formation of smaller size particles (Figure 2d), which is a determining factor in the AIE of fluorescence of compound **7**. To further verify our observations, DLS analysis (Figure S17) was performed on samples prepared with different solvent compositions. The analysis revealed an average hydrodynamic diameter of approximately 91.5 nm in pure THF (0% water), confirming the presence of nanoscale assemblies even under these conditions. Upon increasing the water fraction to 90%, the average particle size decreased to approximately 77.8 nm. These results are consistent with the trend observed in the SEM and TEM images.

To investigate the stimuli-responsive behavior of probe **7** toward different metal ions, perchlorate salts of various metal ions such as Na^+, K^+, Ag^+, Ca^{2+}, Mn^{2+}, Fe^{2+}, Co^{2+}, Ni^{2+}, Cu^{2+}, Zn^{2+}, Pb^{2+}, Cd^{2+}, Hg^{2+}, Cr^{3+}, and Fe^{3+} were individually added to a solution of **7** in CH_3CN–H_2O (1:1, v/v, PBS, pH = 7.2). The absorption spectrum of **7** exhibited a distinct band at 650 nm, which remained significantly unchanged upon the addition of most metal ions except Zn^{2+}(Figure S13). Remarkably, in the presence of Zn^{2+}, a pronounced enhancement in the absorption intensity with the appearance of a peak at 670 nm was observed, accompanied by a visible color transition from blue to dark blue. Conversely, Cd^{2+} elicited only negligible spectral changes, with responses substantially weaker than those observed for Zn^{2+}, thereby indicating a high selectivity of probe **7** toward Zn^{2+} over Cd^{2+} and other metal ions. Upon excitation at 600 nm, the Zn^{2+}-treated solution of **7** displayed an emission band originally centered at 670 nm, which red-shifted to 685 nm along with an emergence of a strong red fluorescence (Figure S14). In contrast, other metal ions did not produce any significant fluorescence response, while Cd^{2+} induced only a negligible change. In addition, interference experiments in the presence of competing metal ions were performed (Figure S14b), and the response toward Zn^{2+} was largely retained, supporting the selectivity of the probe under mixed-metal conditions.

To further assess the Zn^{2+} sensing ability of **7**, both UV–Vis and fluorescence titration experiments (Figure 3) were performed. Incremental addition of Zn^{2+} (0–10 equivalents) to a 10 μM solution of **7** led to a pronounced enhancement in the absorption intensity, followed by a slight red shift to 670 nm, which remained constant thereafter, upon further addition of 15 eq. of Zn^{2+} (Figure 3a). Correspondingly, fluorescence titration of **7** (1 μM) in CH_3CN–H_2O (1:1, v/v, PBS, pH = 7.1) revealed progressive enhancement of the emission intensity at 670 nm, accompanied by a slight red shift to 685 nm. The fluorescence response plateaued beyond 10 equivalents of Zn^{2+}, indicating saturation (Figure 3b). In contrast, the corresponding diterpyridyl-BODIPY analogs **8** and **9** exhibited negligible photophysical changes upon Zn^{2+} addition (Figure S15), highlighting the superior responsiveness of the hexaterpyridyl system. Hence, the compound **7** demonstrated a strong ability to bind and respond to Zn^{2+} through both chromo-fluorogenic, indicating its suitability for the quantitative detection of $Zn^{2+}$with LOD value of 21.81 nM (Figure S16). Zn^{2+} binds to the terpyridine units, which act as tridentate ligands coordinating through nitrogen atoms to form a stable complex, as widely reported in the literature [35–39]. Upon coordination, the terpyridine moieties facilitate charge

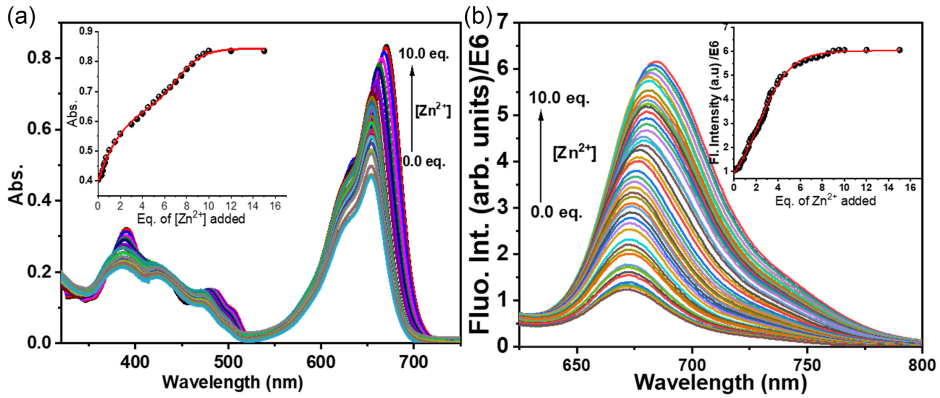

FIGURE 3 | (a) Absorption and (b) fluorescence spectral profile of **7,** respectively, as a function of the concentration of Zn^{2+} added, and (inset) plot of absorption and fluorescence monitored at maximum wavelength versus equivalent of Zn^{2+} added. Conditions: absorption: [**7**] = 10 μM and emission [**7**] = 1 μM, RT, $\lambda_{ex.}$ = 600 nm, b.p. = 5 nm.

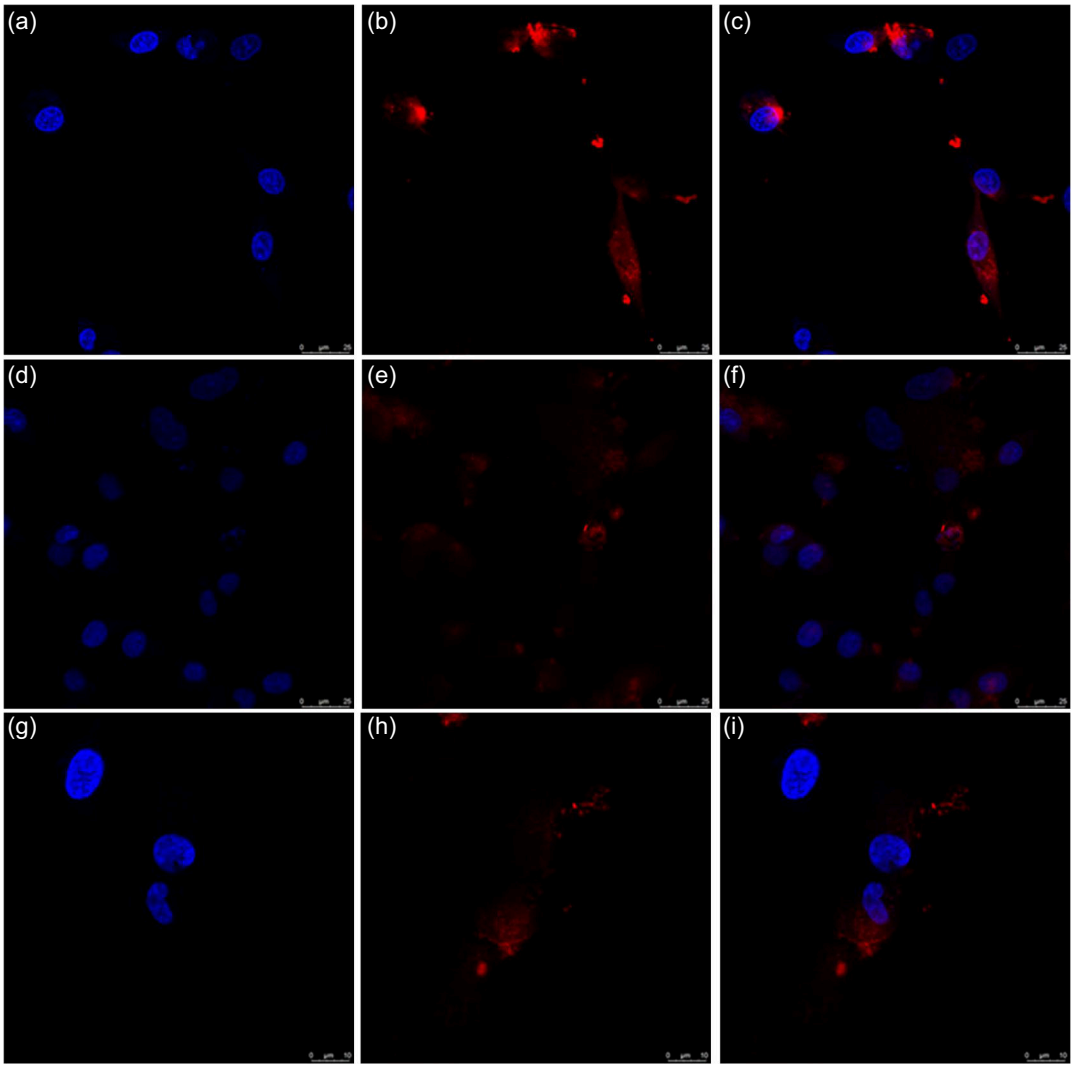

FIGURE 4 | Confocal laser scanning microscopy images of U87 cells treated with compounds **7** (a–c), **8** (d–f), and **9** (f–g), with PBS-treated cells used as the control. Cell nuclei were stained with Hoechst 33 342 (blue), and the red fluorescence corresponds to compounds **7**–**9**. Scale bar: 20 μm.

transfer, enhancing the ICT process and causing a red shift in the fluorescence emission. To verify Zn^{2+} binding, the zinc complex was prepared by reacting **7** with $ZnCl_2$ (10 equiv.) and characterized by HRMS. The HRMS spectrum (Figure S19) showed a peak at m/z = 2927.9399, confirming the formation of the **7**–Zn^{2+} complex. This result supports the proposed coordination of Zn^{2+} to the terpyridine units of **7**. Owing to its hexaterpyridyl architecture, ligand **7** could potentially coordinate up to six Zn^{2+} ions through its six terpyridine moieties, leading to multimetallic or higher-order metal-coordinated assemblies.

However, the exact coordination stoichiometry, extent of metal binding, and coordination geometry could not be conclusively determined from the present data and would require further detailed structural investigations.

To examine intracellular internalization, U87 cells were incubated with compounds **7–9** for 12 h and subsequently analyzed using confocal laser scanning microscopy [40]. The cellular uptake and endosomal accumulation of the compounds were visualized through their intrinsic red fluorescence. As shown in Figure 4, cells treated with compound **7** (Figure 4a–c) exhibited markedly stronger red fluorescence compared to those treated with compounds **8** (Figure 4d–f) and **9** (Figure 4g–i), which is attributed to its higher fluorescence intensity. The merged confocal images further demonstrate that pronounced red fluorescence was observed predominantly in the compound **7**, reflecting its higher fluorescence quantum yield and indicating relatively efficient cellular uptake via endocytosis.

The biocompatibility of compound **7** was evaluated using 3T3 (normal) and U87 (cancer) cell lines. Cells were independently treated with selected concentrations of compounds **7–9** for two different incubation periods, and cell viability was assessed using the MTT assay [35]. All three compounds exhibited minimal cytotoxicity, maintaining more than 90% relative cell viability across the tested concentration range in both U87 (Figure 5a) and 3T3 (Figure 5b) cell lines, confirming their excellent biocompatibility.

The phototoxic effects of compounds **7–9** at varying concentrations were further examined under 660 nm laser irradiation (1.5 W/cm^2) for 3 min using the MTT assay. As illustrated in Figure 5c, none of the compounds caused noticeable cytotoxicity in the absence of laser exposure. However, laser irradiation resulted in a significant reduction in cell viability, following the trend: compound **9** > **8** > **7**. This enhanced phototoxic effect is attributed to the higher fluorescence intensity of compound **7**, leading to increased PDT-mediated cell damage.

Density functional theory (DFT) calculations were performed to gain insight into the molecular geometries and electronic properties of compounds **7–9** (Figures 6, S14, and Tables S1–S3). Geometry optimizations were carried out at the B3LYP/6-31G(d, p) level of theory [41]. The optimized ground-state (S_0) structures of compounds **7–9**, together with their selected frontier molecular orbital (FMO) diagrams, are shown in Figure 6. Notably, in all three compounds, the terpyridine unit consistently adopts a transoid conformation. FMO analysis reveals distinct differences in electronic density distribution among compounds **7–9**. In all cases, the highest occupied molecular orbital (HOMO) is primarily delocalized over the dipyrrin core; however, the extent of conjugation with

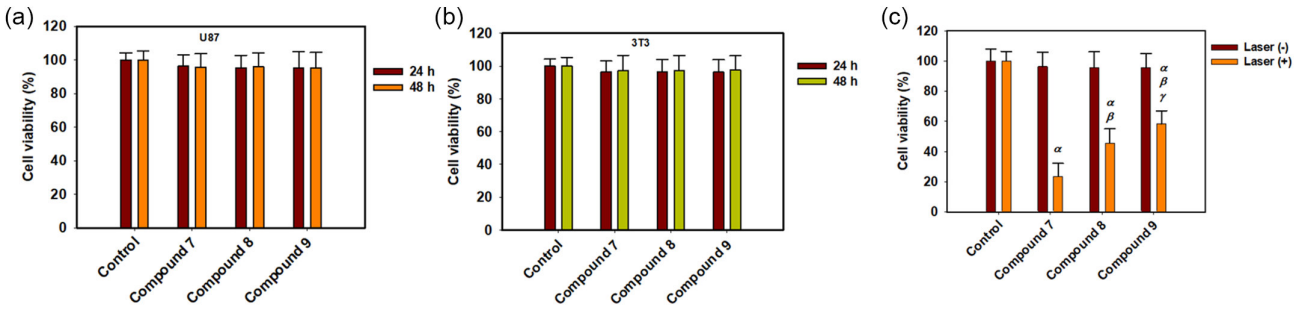

FIGURE 5 | The biocompatibility of compounds **7–9** toward (a) U87 and (b) 3T3 fibroblast (compound concentration = 100 μg/mL) at 24 and 48 h, and (c) in vitro cytotoxicity toward U87 after treating with compounds **7–9** without laser (Laser−) or with laser (Laser+) far-red laser irradiation (660 nm). $^{\alpha}p < 0.05$ compared to control (Laser+), $^{\beta}p < 0.05$ compared to compound 7 (Laser+), and $^{\gamma}p < 0.05$ compared to compound 8 (Laser+).

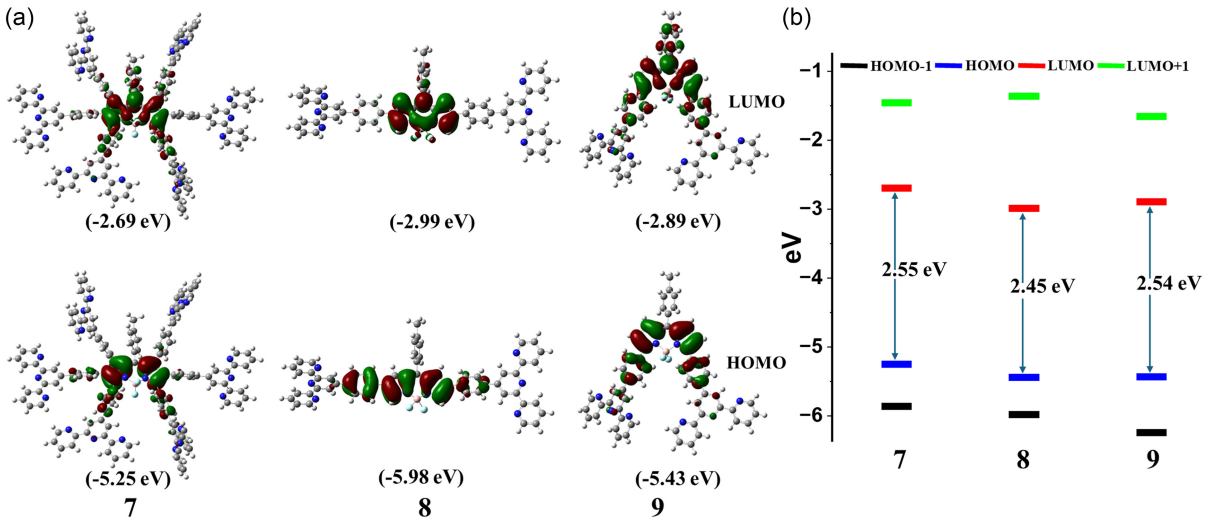

FIGURE 6 | (a) Frontier molecular orbital (HOMO and LUMO) diagrams of compounds **7–9**, and (b) the FMOs energy values of compounds **7–9**.

the phenyl substituents varies. For compound **7**, the HOMO is delocalized over the dipyrrin unit and both α-conjugated phenyl rings, with minor contribution from the β-conjugated phenyl rings. In compound **8**, the HOMO density extends mainly onto both β-conjugated phenyl rings, whereas in compound **9** it is distributed predominantly over both α-conjugated phenyl rings. Similarly, the lowest unoccupied molecular orbital (LUMO) exhibits compound-dependent localization. In compound **7**, the LUMO is delocalized over the dipyrrin framework, including the *meso*-tolyl group and both α-conjugated phenyl rings, with a small contribution from one β-conjugated phenyl ring. For compound **8**, the LUMO is largely confined to the dipyrrin unit. In compound **9**, the LUMO density is localized on the dipyrrin core together with both α-conjugated phenyl rings and the meso-tolyl group. These variations in HOMO and LUMO distributions highlight the distinct electronic characteristics of each compound arising from their structural differences. Additionally, compound **7** exhibits more stabilized HOMO and LUMO energy levels compared to compounds **8** and **9**.

3 | Conclusion

In summary, we have developed a sterically crowded hexaterpyridyl-functionalized BODIPY platform that unifies AIE, far-red fluorescence, metal-ion recognition, and bioimaging within a single molecular scaffold. Installation of six terpyridine units at the α/β positions creates pronounced steric crowding, effectively restricting intramolecular motion and thereby activating robust AIE behavior while simultaneously enabling sensing of Zn^{2+} ion with LOD value of 21.81 nM. Systematic aggregation studies in THF/water mixtures revealed a marked fluorescence enhancement accompanied by emission modulation, which was directly correlated with the formation of well-defined spherical nanoaggregates, as confirmed by TEM and SEM analyses. Comparative investigations with regioselective α,α- and β,β-diterpyridyl analogs clearly demonstrate that multiligand steric congestion is a decisive factor governing aggregation morphology, photophysical performance, and biological activity. Notably, the hexaterpyridyl derivative exhibits superior cellular uptake and bright intracellular fluorescence, together with excellent biocompatibility in both normal and cancer cell lines. Under far-red laser irradiation, this compound further displays significantly enhanced phototoxicity relative to its diterpyridyl counterparts, while remaining essentially noncytotoxic in the dark, highlighting its promise for photodynamically driven therapeutic applications. DFT calculations provide additional insight into the structure–property relationships underpinning these observations. Collectively, this work establishes a versatile molecular design strategy for sterically crowded, multidentate BODIPY fluorophores that seamlessly integrate AIE, metal-ion sensing, and bioimaging capabilities. The present platform offers a compelling blueprint for constructing next-generation multifunctional luminogens and opens new avenues toward advanced applications in supramolecular assemblies, optoelectronic materials, and biomedical diagnostics and therapy.

4 | Experimental Section

Compounds **1** [42], **1-Br$_2$** [42], **1-Br$_6$** [42], and **Terp-B(OH)$_2$** [43] were synthesized by following the previously reported procedures.

4.1 | Synthesis of 7

To the solution of **1-Br$_6$** (75 mg, 0.10 mmol) and Terp-B(OH)$_2$ (540 mg, 2 mmol) in a mixture of toluene: THF: water (1:1:1, 30 mL), the catalyst Pd(dtbpf)Cl$_2$ (2 mol%), and Na_2CO_3 (157 mg, 1.50 mmol) were added and the reaction mixture was stirred at 80°C under nitrogen atmosphere for 32 h. The progress of the reaction was monitored by TLC analysis and absorption spectroscopy. The solvent was removed under reduced pressure, and the resulted crude compound was purified by silica column chromatography using DCM /MeOH (1/9) with TEA (0.5%) to afford pure compound **7** as a green crystalline solid.

Yield: 25 %; ^{1}H NMR(400 MHz, $CDCl_3$) δ_H 8.81–8.62 (33 H, m), 7.88 (24 H, ddd, *J* 23.2, 19.4, 8.4), 7.73 (6 H, t, *J* 7.9), 7.49 (3 H, d, *J* 7.9), 7.40–7.31 (10 H, m), 7.26 (3 H, s), 7.22 (3 H, s), 2.59 (3 H, s); ^{13}C NMR (101 MHz, $CDCl_3$) δ 165.0, 151.6, 147.5, 137.2, 133.5, 131.7, 130.5, 129.0, 128.3, 127.7, 123.9, 117.9, 115.6, 106.0, 97.1, 21.4; ^{11}B NMR (128 MHz, $CDCl_3$) δ 1.37 (t, *J* = 31.9 Hz); ^{19}F NMR (377 MHz, $CDCl_3$) δ −141.09 (dd, *J* = 64.3, 32.1 Hz); HRMS (ESI-TOF): $(m/z)^+$ calcd. for $C_{142}H_{91}BF_2N_{20}$ $[M + H]^+$ 2125.7875; found 2125.7857.

4.2 | Compound 8

To the solution of **1-Br$_2$** (57 mg, 0.13 mmol) and Terp-B(OH)$_2$ (141 mg, 0.40 mmol) in a mixture of toluene: THF: water (1:1:1, 30 mL), the catalyst Pd(PPh$_3$)$_4$ (30 mg, 0.026 mmol), and Na_2CO_3 (55 mg, 0.52 mmol) were added and the reaction mixture was stirred at 80°C under nitrogen atmosphere for 8 h. The crude compound was purified by silica column chromatography using petroleum ether/ethyl acetate (1:9) to afford compound **8** as a red crystalline solid.

Yield: 40 %, ^{1}H NMR; (400 MHz, $CDCl_3$) δ_H 8.78 (8 H, d, *J* 6.6), 8.71 (3 H, d, *J* 7.9), 8.41 (2 H, s), 7.97 (4 H, d, *J* 7.6), 7.92 (4 H, t, *J* 7.5), 7.71 (4 H, d, *J* 7.5), 7.65 (2 H, d, *J* 7.2), 7.49 (2 H, d, *J* 7.4), 7.45–7.36 (5 H, t), 7.24 (2 H, s), 2.59 (3 H, s); ^{13}C NMR (101 MHz, $CDCl_3$) δ 153.2, 152.1, 148.8, 142.5, 140.6, 140.3, 137.9, 136.1, 134.8, 134.0, 133.7, 132.4, 131.5, 130.5, 129.1, 128.5, 127.6, 126.3, 125.5, 123.1, 122.5, 121.7, 121.4, 120.0, 119.1, 117.4, 117.3, 21.9; HRMS (ESI-TOF): $(m/z)^+$ calcd. for $C_{58}H_{39}BF_2N_8$ $[M + H]^+$ 897.3359; found 897.3419.

4.3 | Compound 9

To the solution of α,α-di(bromo)-BODIPY (60 mg, 0.13 mmol) and Terp-B(OH)$_2$ (141 mg, 0.40 mmol) in a mixture of toluene: THF: water (1:1:1, 30 mL), the catalyst Pd(PPh$_3$)$_4$ (30 mg, 0.026 mmol), and Na_2CO_3 (55 mg, 0.52 mmol) were added and the reaction mixture was stirred at 80°C under nitrogen atmosphere for 36 h. The crude compound was purified by silica column chromatography using petroleum ether/ethyl acetate (65:35) to afford compound **9** as a red crystalline solid.

Yield: 34 % (39 mg); ^{1}H NMR (400 MHz, $CDCl_3$) δ 8.80 (s, 2H), 8.70 (d, *J* = 4.8 Hz, 4H), 8.67 (d, *J* = 1.1 Hz, 4H), 8.65 (s, 1H), 8.08 (d, *J* = 8.5 Hz, 4H), 8.02 (d, *J* = 8.6 Hz, 4H), 7.88 (d, *J* = 1.8 Hz, 2H), 7.86 (d, *J* = 1.8 Hz, 2H), 7.84 (d, *J* = 1.8 Hz, 1H), 7.53 (d, *J* = 8.0 Hz, 2H), 7.37 (d, *J* = 7.7 Hz, 2H), 7.34 (d, *J* = 1.1 Hz, 2H), 7.33 (d, *J* = 1.2 Hz, 2H), 7.31 (d, *J* = 1.2 Hz, 2H), 6.97 (d, *J* = 4.2 Hz, 2H), 6.75 (d,

$J = 4.3$ Hz, 2H), 2.51 (s, 3H), ^{13}C NMR (101 MHz, $CDCl_3$) δ 157.96, 156.32, 155.85, 149.51, 149.15, 140.67, 139.22, 136.81, 133.28, 130.72, 130.12, 129.08, 127.11, 123.76, 121.32, 118.88, 21.49, ^{11}B NMR (128 MHz, $CDCl_3$) δ 1.51 (t, $J = 31.9$ Hz); ^{19}F NMR (377 MHz, $CDCl_3$) δ −132.22 (dd, $J = 64.3$, 32.1 Hz); HRMS (ESI-TOF): $(m/z)^+$ calcd. for $C_{58}H_{39}BF_2N_8$ $[M + H]^+$ 897.3359; found 897.3286.

Funding

The authors have nothing to report.

Conflicts of Interest

The authors declare no conflicts of interest.

Data Availability Statement

The data that support the findings of this research study are available in the supplementary material of this article.

References

1. Y. Ye, M. He, L. Wang, X.-C. Shen, and H. Chen, "Unexpected Dual-Functional Cyanine Fluorophores: NIR Multifunctional Fluorescent Probes for Simultaneous Monitoring of Mitochondrial Cysteine /Viscosity during Kidney Ferroptosis In Vivo," *Sensors and Actuators B: Chemical* 396 (2023): 134600.

2. M. M. Zafar, R. Yadav, A. Singh, N. Tyagi, A. Samanta, and R. K. Mishra, "Tetrasubstituted Imidazole-Based Multifunctional Fluorophores: Trace Water Detection and Lipid Droplet (LD) Imaging Studies," *Chemical Communications* 61 (2025): 9091–9094.

3. W. Zhang, Y. Lv, F. Huo, Y. Yun, and C. Yin, "Photoactivation Inducing Multifunctional Coupling of Fluorophore for Efficient Tumor Therapy In Situ," *Advanced Materials* 36 (2024): e2314021.

4. F. Ding, Y. Zhan, X. Lu, and Y. Sun, "Recent Advances in Near-Infrared II Fluorophores for Multifunctional Biomedical Imaging," *Chemical Science* 9 (2018): 4370–4380.

5. W. Liu, Z. Chen, C.-J. Zheng, et al., "A Novel Nicotinonitrile Derivative as an Excellent Multifunctional Blue Fluorophore for Highly Efficient Hybrid White Organic Light-Emitting Devices," *Journal of Materials Chemistry C* 3 (2015): 8817–8823.

6. I. S. Yadav and R. Misra, "Design, Synthesis and Functionalization of BODIPY Dyes: Applications in Dye-Sensitized Solar Cells (DSSCs) and Photodynamic Therapy (PDT)," *Journal of Materials Chemistry C* 11 (2023): 8688–8723.

7. A. Loudet and K. Burgess, "BODIPY Dyes and Their Derivatives: Syntheses and Spectroscopic Properties," *Chemical Reviews* 107 (2007): 4891–4932.

8. P. Kaur and K. Singh, "Recent Advances in the Application of BODIPY in Bioimaging and Chemosensing," *Journal of Materials Chemistry C* 7 (2019): 11361–11405.

9. N. A. Bumagina and E. V. Antina, "Review of Advances in Development of Fluorescent BODIPY Probes (chemosensors and Chemodosimeters) for Cation Recognition," *Coordination Chemistry Reviews* 505 (2024): 215688.

10. M. S. Iqbal, H. Ahmad, C. Yu, H. Huang, and B. Guo, "Near-Infrared BODIPY-Based Theranostic Agents for Photothermal and Combinatory Therapy of Cancers, where Do We Stand in Year 2025," *Coordination Chemistry Reviews* 541 (2025): 216781.

11. L. Vellanki and R. Mangalampalli, "Polyarylated Boron-Dipyrromethenes Containing Three Different Types of Aryl Groups," *RSC Advances* 4 (2014): 44327–44336.

12. L. Vellanki and R. Mangalampalli, "Photophysical and Electrochemical Properties of Sterically Crowded Polyarylated Boron-Dipyrromethenes," *Chemical Physics Letters* 564 (2013): 93–97.

13. J. Li, B. Hu, G. Hu, X. Li, P. Lu, and Y. Wang, "An Efficient Synthesis of Heptaaryldipyrromethenes From Tetraarylcyclopentadienones and Ammonium Acetate and Their Extension to the Corresponding BODIPYs," *Organic & Biomolecular Chemistry* 10 (2012): 8848–8859.

14. L. Vellanki and R. Mangalampalli, "Synthesis of Sterically Crowded Polyarylated Boron-Dipyrromethenes," *The Journal of Organic Chemistry* 76 (2011): 8466–8471.

15. M. R. Suman and A. S. J. Chakravarthy, "Review on New Horizons of Aggregation Induced Emission: From Design to Development," *Materials Chemistry Frontiers* 5 (2021): 1541–1584.

16. H. Wang, Q. Li, P. Alam, et al., "Aggregation-Induced Emission (AIE), Life and Health," *ACS Nano* 17 (2023): 14347–14405.

17. J. Mei, N. L. C. Leung, R. T. K. Kwok, J. W. Y. Lam, and B. Z. Tang, "Aggregation-Induced Emission: Together We Shine, United We Soar!," *Chemical Reviews* 115 (2015): 11718–11940.

18. D. Yan, D. Wang, and B. Z. Tang, "In Vivo, Clinical and Translational Aspects of Aggregation-Induced Emission," *Nature Reviews Bioengineering* 3 (2025): 976–991.

19. X. Tian, Q. Zhang, M. Zhang, et al., "Probe for Simultaneous Membrane and Nucleus Labeling in Living Cells and *In Vivo* Bioimaging Using a Two-Photon Absorption Water-Soluble Zn(Ii) Terpyridine Complex with a Reduced π-Conjugation System," *Chemical Science* 8 (2017): 142–149.

20. W. Zhou, X. Wang, M. Hu, C. Zhu, and Z. Guo, "A Mitochondrion-Targeting Copper Complex Exhibits Potent Cytotoxicity against Cisplatin-Resistant Tumor Cells through Multiple Mechanisms of Action," *Chemical Science* 5 (2014): 2761–2770.

21. R. Kushwaha, A. Upadhyay, S. Saha, et al., "Cancer Phototherapy by CO Releasing Terpyridine-Based Re(i) Tricarbonyl Complexes *via* ROS Generation and NADH Oxidation," *Dalton Transactions* 53 (2024): 13591–13601.

22. R. Abhijnakrishna, K. Magesh, A. Ayushi, and S. Velmathi, "Advances in the Biological Studies of Metal-Terpyridine Complexes: An Overview From 2012 to 2022," *Coordination Chemistry Reviews* 496 (2023): 215380.

23. S. F. Kainat, M. B. Hawsawi, E. U. Mughal, et al., "Recent Developments in the Synthesis and Applications of Terpyridine-Based Metal Complexes: A Systematic Review," *RSC Advances* 14 (2024): 21464–21537.

24. C. Wei, Y. He, X. Shi, and Z. Song, "Terpyridine-Metal Complexes: Applications in Catalysis and Supramolecular Chemistry," *Coordination Chemistry Reviews* 385 (2019): 1–19.

25. Y. Li, Z. Gu, T. He, et al., "Terpyridyl-Based Triphenylamine Derivatives with Aggregation-Induced Emission Characteristics for Selective Detection of Zn2+, Cd2+ and CN− Ions and Application in Cell Imaging," *Dyes and Pigments* 173 (2020): 107969.

26. M. Kong, Y. Zhu, W. Du, et al., "A Series of Terpyridine Derivatives for Aggregation-Induced Emission, Two-Photon Absorption and Mitochondrial Targeting," *Dyes and Pigments* 158 (2018): 225–232.

27. S. Wang, Y. Lin, C. Zhang, et al., "Fine Tuning of Multiphoton AIE Emission Behavior, Organelle Targeting, and Fluorescence Lifetime Imaging of Terpyridine Derivatives by Alkyl Chain Engineering," *Analytical Chemistry* 94 (2022): 4335–4342.

28. T. Ganguly, P. Pal, A. Paul, and S. Baitalik, "Synthesis and Manifold but Controllable Emission Switching of Stilbene-Appended Polyaromatic Terpyridine Derivatives via Aggregation and Trans–cis Isomerization," *Journal of Photochemistry and Photobiology A: Chemistry* 430 (2022): 113966.

29. J. Yuan, Z. Jiang, D. Liu, Y. Li, and P. Wang, "Synthesis and Photophysical Properties of Multi-Ru^{2+} Terpyridine Complexes: From Di-Nuclear Linear to Star-Shaped Hexa-Nuclear Architectures," *Inorganic Chemistry Frontiers* 3 (2016): 268–273.

30. S. Sezer, S. Köytepe, A. Gültek, and T. Seçkin, "Synthesis and Stimuli-Responsive Properties of Metallo-Supramolecular Phosphazene Polymers Based on Terpyridine Metal Complexes," *Journal of Inorganic and Organometallic Polymers and Materials* 31 (2021): 3389–3405.

31. M. Trivedi, G. Singh, A. Kumar, and N. P. Rath, "Syntheses, Characterization, and Structural Studies of Copper(i) Complexes Containing 1,1′-Bis(di-Tert-Butylphosphino)ferrocene (dtbpf) and Their Application in Palladium-Catalyzed Sonogashira Coupling of Aryl Halides," *Dalton Transactions* 43 (2014): 13620–13629.

32. X. Chen, J. Zhou, Z. Xie, and Y. Ma, "Excitons in Confined Molecular Aggregates," *Information & Functional Materials* 1 (2024): 68–86,

33. Y. Lin, J. Zhang, W.-J. Wang, et al., "Pyrene-Based Aggregation-Induced Emission: A Bridge Model to Regulate Aggregation," *Innovation* 6 (2025): 100884.

34. P. Bhandari, S. Ahmed, R. Saha, and P. S. Mukherjee, "Enhancing Fluorescence in Both Solution and Solid States Induced by Imine Cage Formation," *Chemistry – A European Journal* 30 (2024): e202303101.

35. J. Harathi, R. S. Kumar, S. K. A. Kumar, D. Saravanakumar, S. Senthilkumar, and K. Thenmozhi, "Terpyridine-Zn(II) Based Water-Soluble Fluorescent Probes for Selective Detection of Pyrophosphate Ions in Aqueous Medium and Its Bioimaging Application in Living Cells," *Sensors and Actuators B: Chemical* 390 (2023): 133967.

36. T.-W. Hsu, H.-C. Hsu, H.-Y. Chan, and J.-M. Fang, "A Terpyridine Zinc Complex for Selective Detection of Lipid Pyrophosphates: A Model System for Monitoring Bacterial O- and N-Transglycosylations," *The Journal of Organic Chemistry* 85 (2020): 12747–12753.

37. T. Mandal, A. Hossain, A. Dhara, et al., "Terpyridine Derivatives as "turn-on" Fluorescence Chemosensors for the Selective and Sensitive Detection of Zn2+ Ions in Solution and in Live Cells," *Photochemical & Photobiological Sciences* 17 (2018): 1068–1074.

38. X. Bi and Y. Pang, "Optical Response of Terpyridine Ligands to Zinc Binding: A Close Look at the Substitution Effect by Spectroscopic Studies at Low Temperature," *The Journal of Physical Chemistry B* 120 (2016): 3311–3317.

39. R. R. Panicker, S. Joseph, S. Dharani, et al., "A Highly Lipophilic Terpyridine Ligand as an Efficient Fluorescent Probe for the Selective Detection of Zinc(Ii) Ions under Biological Conditions," *Analytical Methods* 17 (2025): 232–245.

40. S. Das, B. S. Dash, Y.-J. Lu, D. Tg, and J.-P. Chen, "Photo-Enhanced Chemotherapy with NIR-Triggered Co-Delivery of IR820-MnO_2 and Quercetin From Targeted Thermosensitive Liposomes for Photo–Chemo Combination Cancer Therapy," *ACS Applied Materials & Interfaces* 17 (2025): 40303–40325.

41. M. J. Frisch, G. W. Trucks, H. B. Schlegel, et al., Gaussian 09, Revision D.01 (Gaussian, Inc., 2009).

42. L. Jiao, W. Pang, J. Zhou, et al., "Regioselective Stepwise Bromination of Boron Dipyrromethene (BODIPY) Dyes," *The Journal of Organic Chemistry* 76 (2011): 9988–9996.

43. C. J. Aspley and J. A. Gareth Williams, "Palladium-Catalysed Cross-Coupling Reactions of Ruthenium Bis-Terpyridyl Complexes: Strategies for the Incorporation and Exploitation of Boronic Acid Functionality," *New Journal of Chemistry* 25 (2001): 1136–1147.

Supporting Information

Additional supporting information can be found online in the Supporting Information section. Supplementary data associated with this article such as characterization data using HRMS, NMR spectra, and, detailed photophysical studies including absorption, emission spectral pattern, DFT data of the compounds are available.